Article

One-Dimensional Photonic Crystals with Different Termination Layer Thicknesses and Very Narrow Bloch Surface Wave and Guided Wave Based Resonances for Sensing Applications

Tomas Fort [1,*] , **Roman Kanok** [2,*] , **Petr Hlubina** [2] , **Pavel Pokorny** [1] and **Jaroslav Sobota** [1]

1 Institute of Scientific Instruments of the Czech Academy of Sciences, Kralovopolska 147, 612 64 Brno, Czech Republic
2 Department of Physics, Technical University Ostrava, 17. Listopadu 2172/15, 708 00 Ostrava-Poruba, Czech Republic
* Correspondence: fortt@isibrno.cz (T.F.); roman.kanok@vsb.cz (R.K.)

Abstract: We demonstrate an efficient sensing of both gaseous and aqueous analytes utilizing Bloch surface waves (BSWs) and guided waves (GWs) excited on a truncated one-dimensional photonic crystal (1DPhC) composed of six TiO_2/SiO_2 bilayers with a termination layer of TiO_2. For the gaseous analytes, we show that 1DPhC can support the GW excited by an *s*-polarized wave and the theoretical shift of the resonance wavelength is linear for small changes in the analyte refractive index (RI), giving a constant RI sensitivity of 87 nm per RI unit (RIU). In addition, for the aqueous analytes, the GW excited by *s*-polarized and BSW by *p*-polarized waves can be resolved and exploited for sensing applications. We compare two designed and realized 1DPhCs with termination layer thicknesses of 60 nm and 50 nm, respectively, and show experimentally the differences in their very narrow reflectance and phase responses. An RI sensitivity and figure of merit as high as 544.3 nm/RIU and 303 RIU^{-1}, respectively, are obtained for the smaller thickness when both *s*- and *p*-polarized BSWs are excited. This is the first demonstration of both very deep BSW-based resonances in two orthogonal polarizations and a very narrow resonance in one of them.

Keywords: photonic crystal; Bloch surface wave; termination layer; reflectance; phase shift; Kretschmann configuration

1. Introduction

One-dimensional photonic crystals (1DPhCs) are structures with a periodic modulation of refractive index (RI) in one spatial dimension. There is an analogy between the propagation of photons in a 1DPhC and the propagation of electrons in a periodic potential of a crystal lattice, and so the concept of band gaps can be adopted [1]. The photonic band gap determines the range of wavelengths of light that cannot propagate through the infinite 1DPhC. In practice, only the truncated 1DPhC can be prepared, which can be represented by a multilayer dielectric structure (MDS), referred to as a Bragg reflector. Within the range of wavelengths corresponding to the photonic band gap, the Bragg reflectors are highly reflective, but they can also guide waves on their surface—the Bloch surface waves (BSWs).

For the excitation of the BSWs, a coupling device has to be used to fulfill the phase-matching condition since the tangential component of the wave vector of the BSWs lies beyond a free space light line. A common way is to use the total internal reflection in a glass prism in the Kretschmann configuration that is widely used to excite the surface plasmon resonance (SPR) [2]. The BSWs show up as a dip in the reflectance spectrum, similar to the SPR, and they also can be exploited in sensing applications. However, contrary to the SPR, narrower resonance dips are related to the BSW since the MDS is composed of low-loss dielectrics, and both *s*- and *p*-polarized waves can be used for the BSW excitation. Moreover, the photonic band gap position and width depend on the MDS geometry and materials, and thus can be varied by the fabrication of the MDS so that ultra-large omnidirectional

photonic band gaps are possible [3]. The sensors based on the BSWs often use not only a wavelength [4–11], but also angular [5,11–14] interrogations. Importantly, sensors utilizing a phase detection have also been demonstrated [15–18].

In this paper, we demonstrate an efficient sensing of both gaseous and aqueous analytes utilizing a MDS composed of 6 TiO_2/SiO_2 bilayers with a termination layer of TiO_2. For the gaseous analyte, we show that the proposed structure can support a guided wave (GW) excited by an s-polarized wave. The GW is accompanied by a reflectance minimum (a dip), which theoretically shifts linearly with small changes in the analyte RI. For the designed and realized 1DPhC and aqueous analytes, the BSWs excited by both s and p-polarized waves can be resolved and utilized for sensing applications. We study the effect of the termination layer thickness on the sensor response by a direct comparison of two MDSs differing only by the termination layer thicknesses. The sensor performance is evaluated in terms of the RI sensitivity and also figure of merit (FOM). We show that the MDS with a termination layer thickness of 50 nm shows both higher sensitivity and FOM than the MDS with a termination layer thickness of 60 nm. In addition, one of the MDSs demonstrates for the first time not only very deep BSW-based resonances in two orthogonal polarizations, but also a very narrow resonance in a single polarization.

2. Materials and Methods

2.1. Structures under Study

A truncated 1DPhC can be represented by a stack of alternating dielectric layers. For the purpose of this study, two MDSs were prepared, each composed of six TiO_2/SiO_2 bilayers with a termination layer of TiO_2. The 1DPhC was inspected by a scanning electron microscope (DualBeam FIB-SEM Helios G4, Thermo Fisher Scientific, Waltham, MA, USA) with images shown in Figure 1. The MDSs differ only in the thickness of the termination layer, which is 60 nm in the first case (MDS_{60}) and 50 nm in the second case (MDS_{50}). The thicknesses of all other TiO_2 and SiO_2 layers are $t_{TiO_2} = 100$ nm and $t_{SiO_2} = 85$ nm, respectively, giving the spatial period $\Lambda = t_{TiO_2} + t_{SiO_2} = 185$ nm. Both MDSs were prepared on a glass substrate by a method of electron beam evaporation; the process is described in detail elsewhere [19].

(a)

(b)
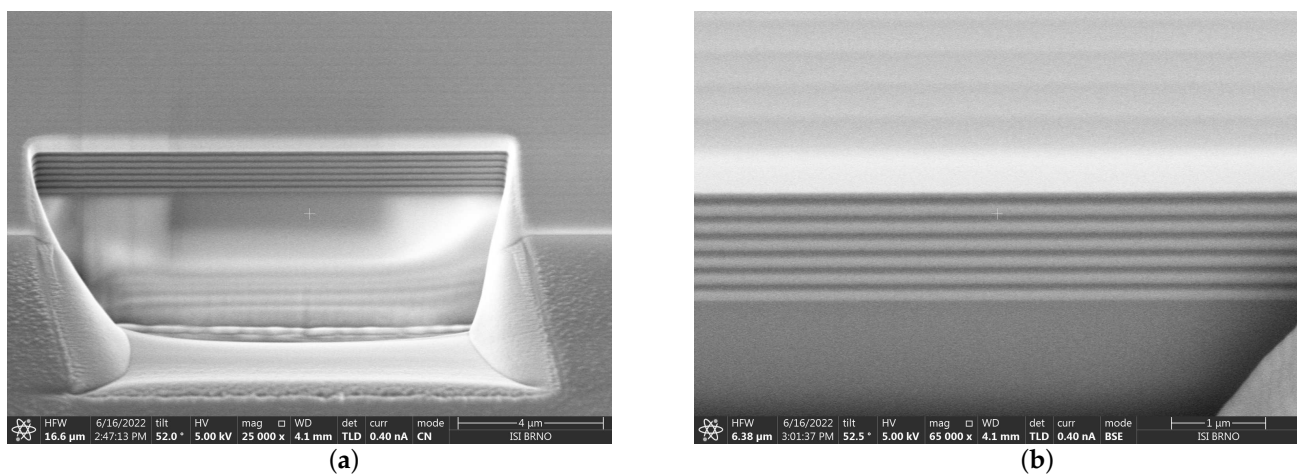
Figure 1. SEM images of the 1DPhC with overall (**a**) and detail (**b**) views.

2.2. Experiment

2.2.1. Experimental Setup

We performed two kinds of experiments with the prepared MDSs. First, we measured interference reflectance $R_{45}(\lambda)$ in the experimental setup shown in Figure 2. During the measurements, one of the MDSs on the glass substrate was attached to a BK7 glass prism (Ealing, Inc., Scotts Valley, CA, USA) using index matching oil (Cargille, $n_D = 1.516$). Using a white light source (halogen lamp HL-2000, Ocean Optics, Orlando, FL, USA), a light

beam was generated and then coupled into an optical fiber and transmitted to a collimating lens. The collimated beam then passed through a linear polarizer (LPVIS050, Thorlabs, Newton, NJ, USA) oriented by the angle $\gamma_P = 45°$ with respect to the plane of incidence and reached the air/prism interface at outer angle of incidence α. The inner angle of incidence θ is given by relation $\theta(\lambda) = 60° - \sin^{-1}[\sin \alpha / n_{BK7}(\lambda)]$, where $n_{BK7}(\lambda)$ is the wavelength-dependent RI of the glass prism. After reflection from the MDS, the beam passed through a linear analyzer (LPVIS050, Thorlabs, Newton, NJ, USA) oriented by the angle $\gamma_A = \pm45°$ with respect to the plane of incidence and it was coupled to a read optical fiber (M15L02, Thorlabs, Newton, NJ, USA) by a microscope objective. As a detector, a compact spectrometer (USB4000, Ocean Optics, Orlando, FL, USA) was used.
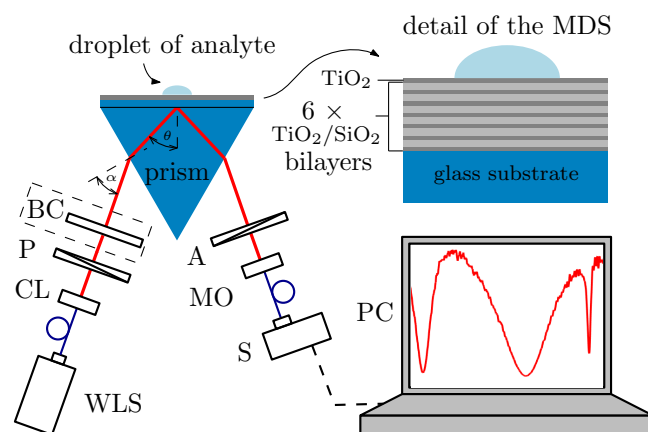
Figure 2. Experimental setup: a MDS in the Kretschmann configuration; white light source (WLS), collimating lens (CL), polarizer (P), birefringence crystal (BC), analyzer (A), microscope objective (MO), spectrometer (S), personal computer (PC), optical fibers (shown as blue lines).

A recorded interference spectrum then followed the equation [9]

$$R_{\pm45}(\lambda) = \frac{1}{4}\{R_s(\lambda) + R_p(\lambda) + 2\sqrt{R_s(\lambda)R_p(\lambda)}\cos[\Delta(\lambda) + \delta_\pm]\}, \tag{1}$$

where $R_s(\lambda)$ and $R_p(\lambda)$ are the spectral reflectances of s- and p-polarized light waves, respectively, $\Delta(\lambda)$ is a phase change between them due to the BSW or GW excitation, and $\delta_\pm$ is a phase term related to the orientation of the analyzer ($\delta_+ = 0$ for $\gamma_A = 45°$ and $\delta_- = \pi$ for $\gamma_A = -45°$). This technique exploits the phase properties of BSWs and GWs to pronounce the related reflectance dips. All measured spectra were normalized with respect to the reflectance $R_p(\lambda)$ measured for air.

Second, we measured an optical phase shift $\phi(\lambda)$ using a spectral interferometric technique. In the measurement, a birefringence quartz prism of thickness 6 mm was included in the experimental setup, which caused an additional phase difference $\Delta_{BC}(\lambda)$ between s- and p-polarized waves. As a result, a spectral interferogram (a channeled spectrum) consisting of fringes could be resolved. Two such interferograms were recorded to determine the phase shift $\phi(\lambda)$. One for the case when the BSW or GW was generated, given by the overall phase $\Phi(\lambda) = \Delta_{BC}(\lambda) + \Delta(\lambda)$, including the phase contributions of both the birefringence crystal and BSW or GW, and second for the case when the waves were not generated, given by $\Phi_R(\lambda) = \Delta_{BC}(\lambda) + \Delta_R(\lambda)$, where $\Delta_R(\lambda)$ is a reference phase term. The reference interferogram was obtained in the setup, not including the MDS. Both interferograms were processed by a windowed Fourier transform [18] to obtain the overall phases $\Phi(\lambda)$ and $\Phi_R(\lambda)$, and then the phase shift $\phi(\lambda) = \Phi(\lambda) - \Phi_R(\lambda)$ was calculated.

2.2.2. Analytes

We performed measurement for room air (temperature $t = 22$ °C, relative humidity RH = 30%) to show a possibility of the sensing of low RI analytes. The effect of temperature changes is not considered, even if it is interesting from the point of view of the thermal

stability of the sensor [20,21]. Next, we prepared six aqueous solutions of NaCl with various RIs n_D in a range of 1.3331–1.3599, corresponding to NaCl concentration ranging from 0 weight percents (wt%) to approximately 10 wt%. The RI was measured with refractometer AR200 (Reichert, New York, NY, USA) at sodium D line ($\lambda_D = 589$ nm) at the room temperature.

2.3. Theoretical Analysis

Measurements are accompanied by the theoretical analysis. The reflectance was calculated by a transfer matrix method (TMM) [22], and we included the following dispersion relation for TiO$_2$ and SiO$_2$ layers [19]

$$n^2(\lambda) = A + \frac{B\lambda^2}{\lambda^2 - C^2},\tag{2}$$

where A, B and C are constants with values $A = 2.7655$, $B = 2.2$, $C = 0.26524$ μm and $A = 1.34836$, $B = 0.756$, $C = 0.10683$ μm for TiO$_2$ and SiO$_2$, respectively, and λ is wavelength in μm. Approximate extinction coefficients of TiO$_2$ and SiO$_2$, $k_{TiO2} = 0.0016$ and $k_{SiO2} = 0.00034$ were included in the calculations.

Dispersion of the water is expressed by the Sellmeier formula [23]

$$n_w^2(\lambda) = 1 + \sum_{n=1}^{4} \frac{D_i \lambda^2}{\lambda^2 - E_i},\tag{3}$$

where D_i and λ_i are constants with values $D_1 = 5.684027565 \times 10^{-1}$, $D_2 = 1.726177391 \times 10^{-1}$, $D_3 = 2.086189578 \times 10^{-2}$, $D_4 = 1.130748688 \times 10^{-1}$, $E_1 = 5.101829712 \times 10^{-3}$ μm^2, $E_2 = 1.821153936 \times 10^{-2}$ μm^2, $E_3 = 2.620722293 \times 10^{-2}$ μm^2 and $E_4 = 1.069792721 \times 10^{-2}$ μm^2 (valid for temperature of 20°).

Both the substrate and the prism are made of BK7 glass, and its dispersion is described by the Sellmeier formula [24]

$$n_{BK7}^2(\lambda) = 1 + \sum_{n=1}^{3} \frac{F_i \lambda^2}{\lambda^2 - G_i},\tag{4}$$

where E_i and λ_i are constants with values $F_1 = 1.03961212$, $F_2 = 0.231792344$, $F_3 = 1.01046945$, $G_1 = 6.00069867 \times 10^{-3}$ μm^2, $G_2 = 2.00179144 \times 10^{-2}$ μm^2, $G_3 = 1.03560653 \times 10^2$ μm^2. Finally, we used the RI of air $n_{air} = 1$.

3. Results

3.1. Reflectances for Air and Water

First, we measured the reflectance ratio $R_{-45}(\lambda)/R_p(\lambda)$ for the MDS$_{60}$, as shown in Figure 3a by the dashed line. In the same figure, we also show the theoretical reflectance ratio for different analyte RIs in a range of 1–1.01 and for the angle of incidence $\theta = 45.5°$, when the reflectances $R_s(\lambda)$ and $R_p(\lambda)$ and the phase difference $\Delta(\lambda)$ are calculated using the transfer matrix method [18].
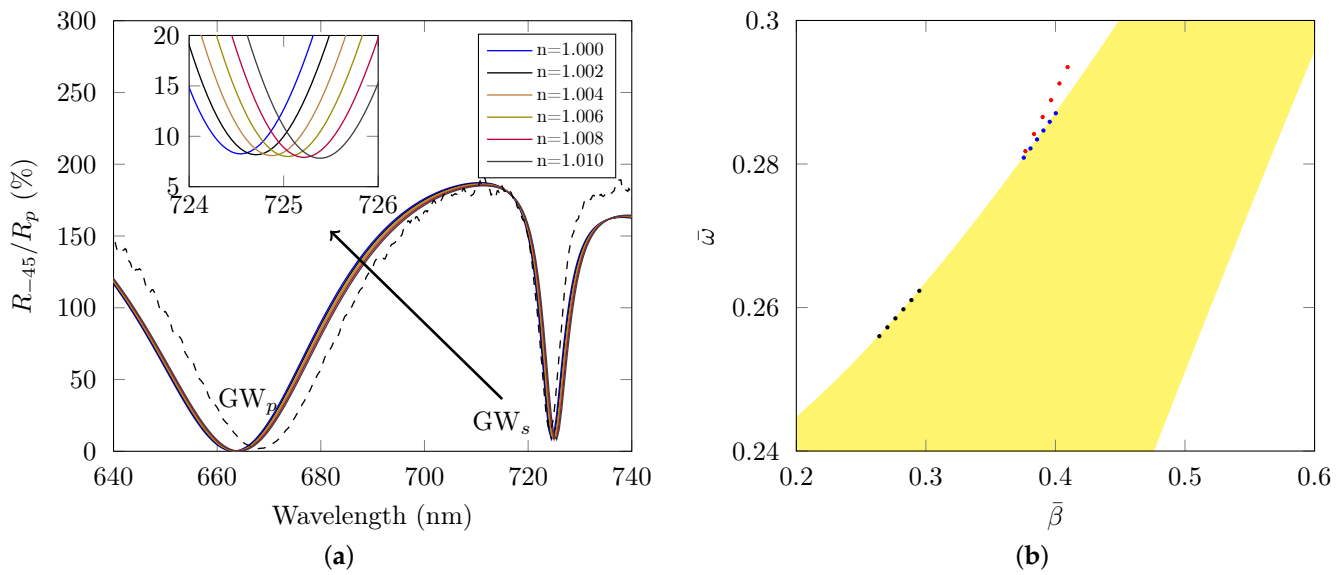
Figure 3. (a) Theoretical reflectance ratio $R_{-45}(\lambda)/R_p(\lambda)$ as a function of wavelength for different RIs of the analyte and the angle of incidence $\theta = 45.5°(\alpha \approx 22°)$. Experimental result for air is shown by the dashed line. **(b)** Band structure of the 1DPhC for *s*-polarized wave with dots corresponding to the GWs for air (black) and water (blue), and the surface waves for water (red).

Analyzing the theoretical results, both reflectance minima correspond to the guided waves. The narrow one at a wavelength of around 725 nm shifts linearly with the RI and is excited by an *s*-polarized wave. We support this by a band structure of an infinite 1DPhC composed of TiO_2/SiO_2 bilayers shown in Figure 3b. The band structure determination is based on solving an eigenvalue problem [1], giving the dependence of the angular frequency ω on the propagation constant β. We use the reduced quantities $\bar{\omega} = \frac{\omega}{c} \frac{\Lambda}{2\pi}$ and $\bar{\beta} = \beta \frac{\Lambda}{2\pi}$ and included the dispersion relations and thicknesses of the thin layers specified in the previous section. The yellow regions represent the allowed bands of frequencies, while the white regions represent the photonic band gaps. The black dots located out of the photonic band gap denote the position of the reflectance dips determined for an angle of incidence θ ranging from 43 to 48°, thus confirming that the appropriate wave is the GW. The dip positions are obtained for a structure containing 100 bilayers of TiO_2/SiO_2 and including no termination layer. Moreover, we compute an optical field distribution [22] within the MDS_{60}, and it is shown in Figure 4a. The field intensity grows with distance from the substrate and it has its maximum value near the MDS/analyte interface. The shape of the field envelope in the crystal, which differs from the exponential one, is due to the GW [25].

By tracing the dip positions (the resonance wavelengths), we obtain a linear dependence on the RI, as shown in Figure 4b. The sensor response can be characterized in terms of the RI sensitivity defined as

$$S_n = \frac{\delta\lambda_R}{\delta n}, \tag{5}$$

where $\delta\lambda_R$ is change in the resonance wavelength and δn is change in the RI of the analyte. In this case, a constant value of 87 nm per RI unit (RIU) is reached. Next, we introduce figure of merit (FOM), which is a parameter that takes into account also a width of the resonance dip and is defined as

$$\text{FOM} = D\frac{S_n}{\text{FWHM}}, \tag{6}$$

where FWHM is full width at half maximum of the resonance dip and D is its depth. In this case, for FWHM = 5.3 nm and $D = 0.96$, FOM has a value of 15.7 RIU^{-1}.

(a)

(b)
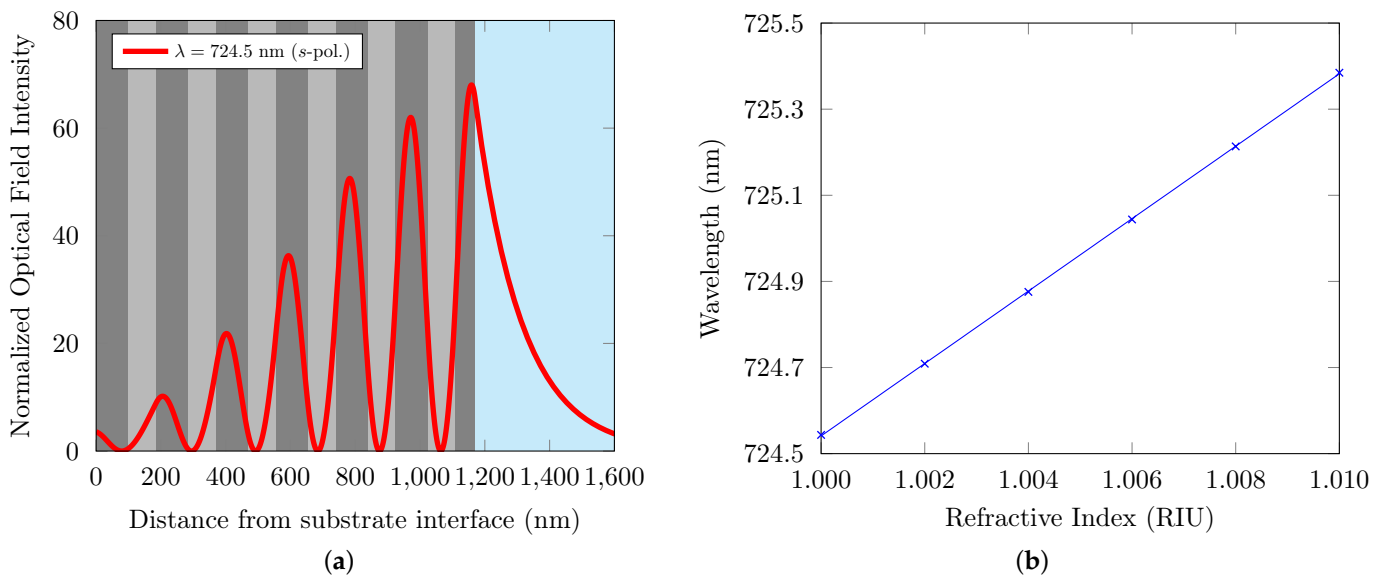
Figure 4. (**a**) Normalized optical field distribution of *s*-polarized wave in the MDS$_{60}$ for air with the RI $n = 1$ and the angle of incidence $\theta = 45.5°$ ($\alpha \approx 22°$). (**b**) Resonance wavelength as a function of analyte RI.

3.2. Water and Aqueous Analytes

It is very well known that an entrance slit width of a spectrometer affects the spectral resolution. Since the resonance dip related to the GW can be very narrow, it can be sometimes problematic to resolve it if the entrance slit is not sufficiently narrow. The resolution of the fiber-optic spectrometers is given by the effective width of the light beam from a core of the read optical fiber [26]. As an example, we used two read optical fibers with core diameters of 25 µm and 50 µm, respectively, to show the difference in the recorded reflectance ratio $R_{+45}(\lambda)/R_p(\lambda)$ for water. As can be seen from Figure 5a, the narrowest dip at a wavelength of approximately 660 nm is almost twice deeper when the fiber with the 25 µm core diameter is used.

(a)

(b)
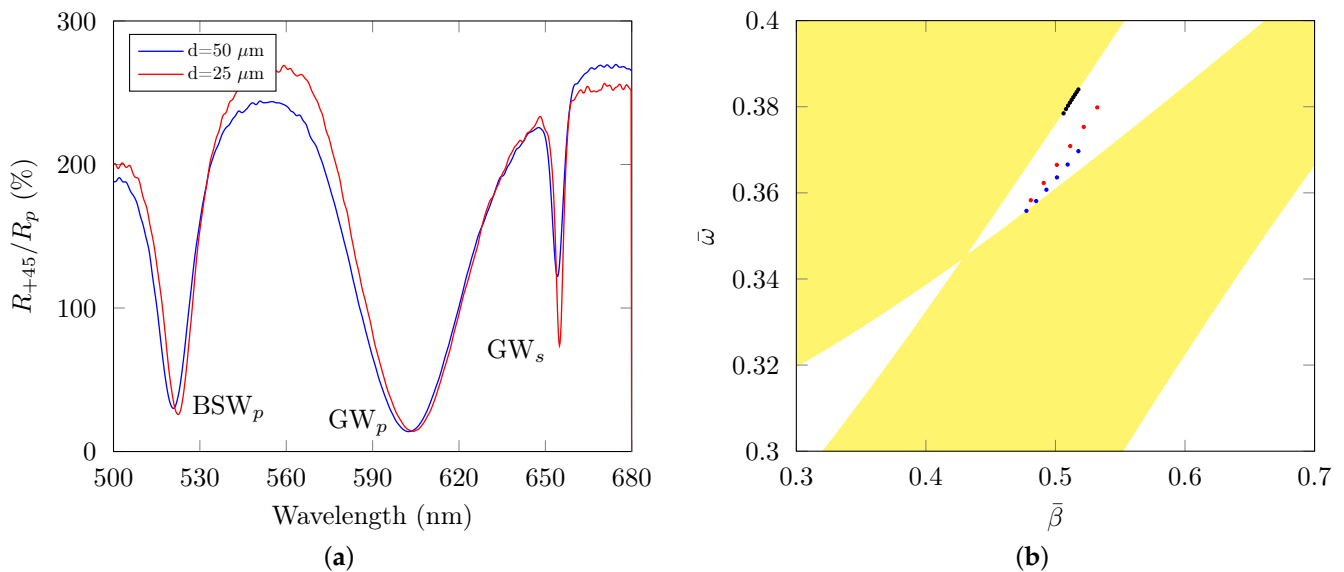
Figure 5. (**a**) Comparison of spectra recorded by the spectrometer employing a read optical fiber of two different core diameters *d*. (**b**) Band structure of the 1DPhC for *p*-polarized wave. Black dots correspond to a multilayer consisting of 450 bilayers, blue and red dots to the MDS including the termination layer with thickness of 60 nm and 50 nm, respectively.

Analyzing the obtained reflectance ratio, one of three resolved dips can be associated with the BSW (labeled as BSW_p), and it is excited by a *p*-polarized wave at a wavelength of approximately 518 nm (for a given angle of incidence), and the remaining two resolved dips can be associated with *s*-polarized waves. In the band structure for the *s*-polarized wave shown in Figure 3b, blue dots out of the photonic band gap represent the guided states for water as the analyte. We can extend our considerations following an approach presented in [27], including also the effect of the termination layer. In the case of the termination layer thickness of 50 nm, the red dots located inside the photonic band gap are obtained. Similarly, for a *p*-polarized wave, we computed the band structure shown in Figure 5b and the reflectance dip positions are depicted by black dots for a multilayer consisting of 450 bilayers. In the case when the termination layer is included in the calculations, blue dots and red dots are obtained for thicknesses of 60 nm and 50 nm in the MDSs, respectively. All the obtained states are located within the photonic band gap.

3.3. Termination Layers with Thicknesses of 60 nm and 50 nm

In this section, we compare the two prepared MDSs in their sensing abilities related to aqueous analytes. In Figure 6a,b, the measured reflectance ratios $R_{+45}(\lambda)/R_p(\lambda)$ are shown for MDS_{60} and MDS_{50}, respectively, for different RIs of the analyte. It can be seen that the reflectance dips related to both *s*- and *p*-polarized waves (BSW or GW) are deeper for the MDS_{60}, but their shift with RI change is smaller than in the case of MDS_{50}.
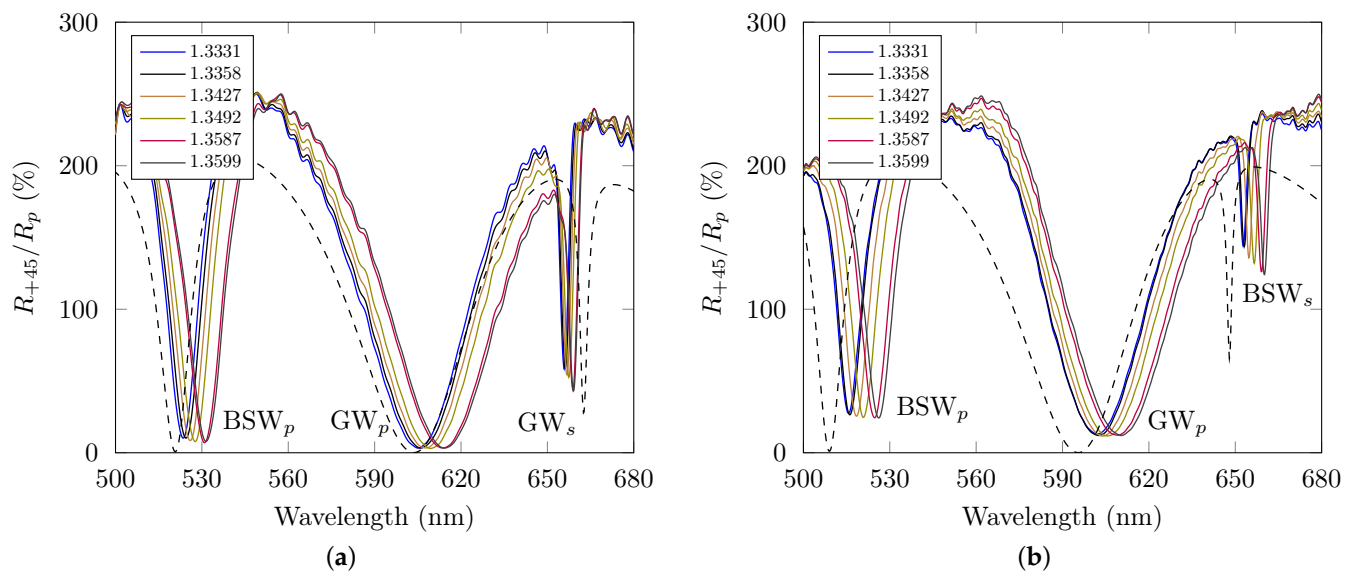
Figure 6. Experimental reflectance ratio $R_{-45}(\lambda)/R_p(\lambda)$ as a function of wavelength for different RIs of the analyte: MDS_{60} (**a**) and MDS_{50} (**b**). The dashed lines are the theoretical results for water.

The theoretical results obtained for pure water with the RI $n = 1.333$ are shown by the dashed lines. For the reflectance dip wavelengths, we calculated the optical intensity distributions within the MDSs, as shown in Figure 7a,b. They clearly illustrate the substantially enhanced optical field with an exponential tail for the MDS_{50} than for the MDS_{60}, and thus increased penetration depth of the field in the analyte. The discrepancy between the theoretical and experimental reflectances can be attributed to the variable thicknesses of all TiO_2 and SiO_2 layers in the real MDS as illustrated for a different MDS in a previous paper [10].
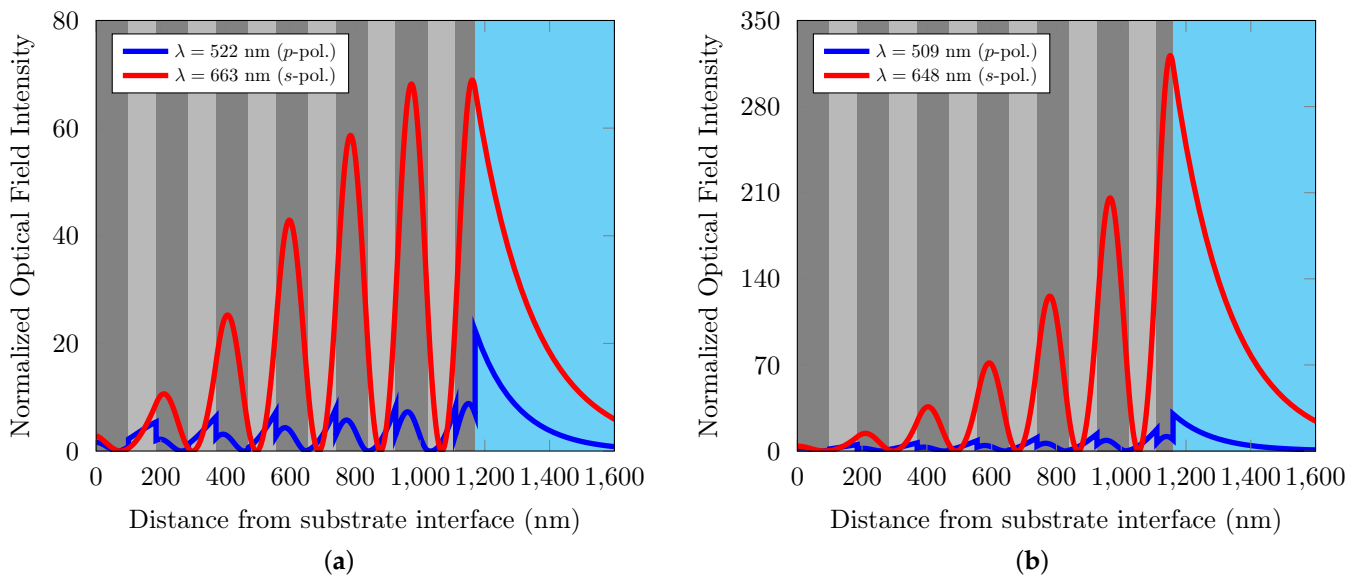
Figure 7. Normalized optical field distribution in MDS at different wavelengths for water and angle of incidence $\theta = 64°$ ($\alpha \approx -6°$): MDS$_{60}$ (**a**) and MDS$_{50}$ (**b**).

In Figure 8a, we show the resonance wavelength of both waves as a function of the RI for both structures. In the case of BSW$_p$, the wavelength shift is about 7.9 nm for MDS$_{60}$ nm and about 11.1 nm for MDS$_{50}$. In the case of the GWs in s polarization, the wavelength shift is about 3.3 nm for MDS$_{60}$ nm and about 7.3 nm for MDS$_{50}$ when the GW is transformed into the BSW.
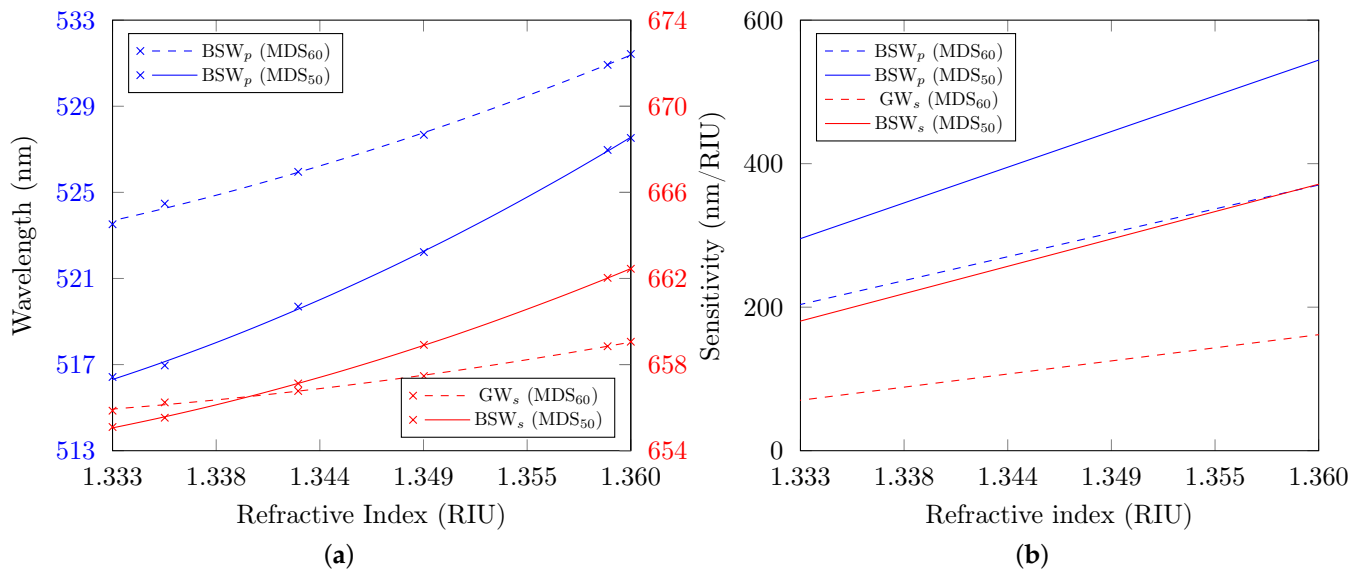
Figure 8. Dependencies of resonance wavelength (**a**) and RI sensitivity (**b**) on RI.

A direct comparison of sensitivities to the RI is shown in Figure 8b. The sensitivities change linearly with the RI, and they are higher for MDS$_{50}$ than for MDS$_{60}$ in the whole RI range. The sensitivity can be further enhanced by decreasing the termination layer thickness, but this is accompanied by the dip depth decrease [19] and thus a smaller FOM increase. A summary of the sensor performance parameters is presented in Table 1.

Table 1. Sensor performance parameters resulting from the reflectance measurements.

	Sensor Parameters for Aqueous Analytes			
Structure	**MDS$_{60}$**		**MDS$_{50}$**	
Wave	**BSW$_p$**	**GW$_s$**	**BSW$_p$**	**BSW$_s$**
S (nm/RIU)	203.8–370.2	70.3–161.7	295.5–544.3	180.7–371.4
FWHM (nm)	13.3	2.7	10	2
D	0.96	0.78	0.96	0.44
FOM (RIU^{-1})	9.2–26.7	20.3–52.1	28.4–52.3	39.8–81.7

Comparing the results with the available ones [4,16,19,28–30], the resonance depths obtained are the greatest; however, the sensitivities are smaller than those for a single polarization [4,16,28], or for both polarizations [19], including also sensors employing fibers [29] and operated in a near infrared spectral region. The sensitivities are close to those for sensors employing a D-shaped optical fiber [30].

3.4. Phase Responses

In this section, we analyze the experimental phase responses of both MDSs. As for the other resonance phenomena, such as a SPR [31,32], an abrupt phase change is related to the BSWs [16], and it can be exploited for sensing applications. In Figure 9a,b, the phase shifts measured for both MDS$_{60}$ and MDS$_{50}$ are shown. While the phase shifts due to the BSW$_p$ are similar in both cases, the phase shifts due to the *s*-polarized waves are substantially different, both in magnitude and sign of its change. Moreover, while a slope of the phase shift due to the *s*-polarized GW is similar for every RI in the case of the MDS$_{60}$, it varies in the case of MDS$_{50}$, when the GW is transformed into the BSW. It is interesting to note that a similar behavior is revealed for a SPR phase response of a simple structure when the thickness of a gold layer is changed [31,32]. In the same figures, we show by dashed lines the theoretical phase $\Delta(\lambda)$ obtained using TMM.
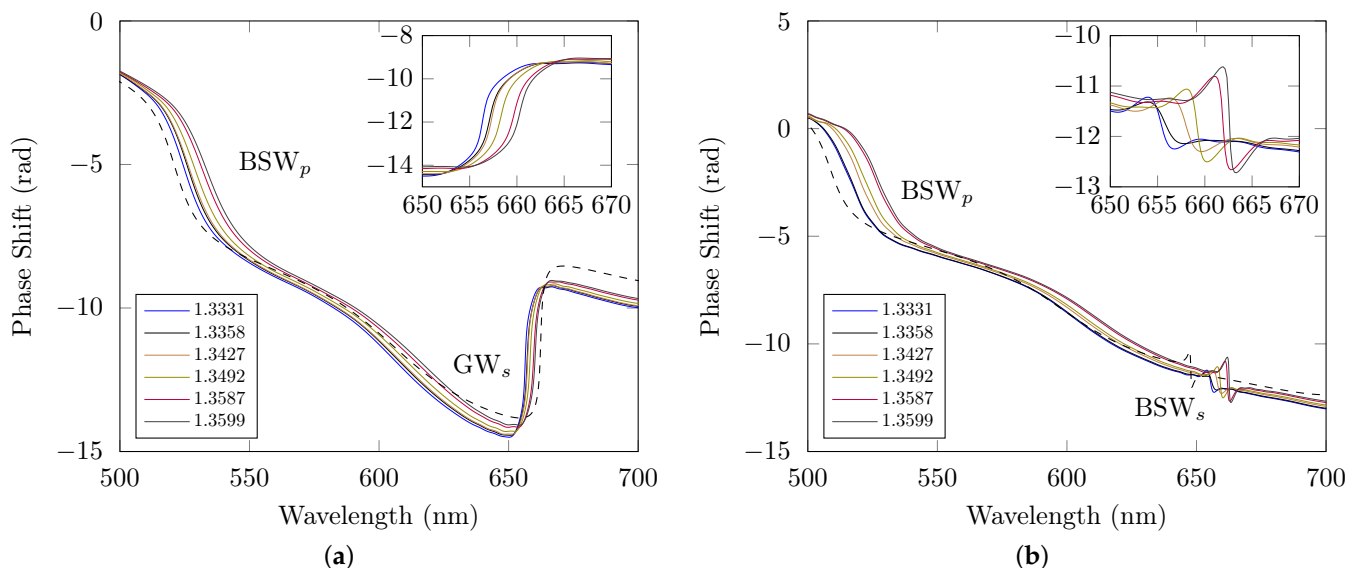
Figure 9. Phase shift as a function of wavelength for different RIs of the analyte: MDS$_{60}$ (**a**) and MDS$_{50}$ (**b**). The dashed lines are the theoretical functions.

In Figure 10a,b, derivatives of the phase shifts are shown for MDS$_{60}$ and MDS$_{50}$, respectively. The derivative peak position can be traced as the RI changes, similar to tracing the reflectance dip.
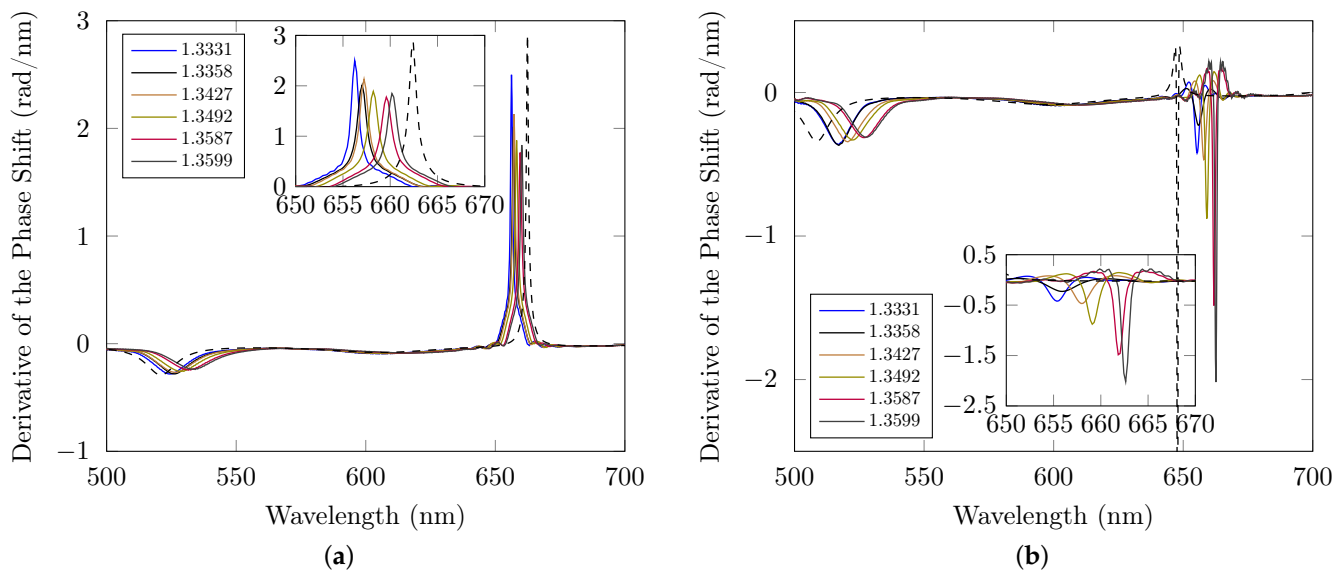
Figure 10. Derivative of the phase shift as a function of wavelength for MDS_{60} (**a**) and MDS_{50}(**b**). The dashed lines are the theoretical functions.

In Figure 11a, we show the wavelengths related to the derivative peaks of wave in both polarizations as functions of the RI for both structures. In the case of BSW_p, the wavelength shift is about 9 nm for MDS_{60} nm and about 10.9 nm for MDS_{50}. In the case of the *s*-polarized GW, the wavelength shift is about 3.9 nm for MDS_{60} nm and about 7.1 nm for MDS_{50}, when the GW is transformed into the BSW. Sensitivities to the RI are compared in Figure 11b. As in the case of reflectance, the sensitivities linearly increase with the RI and are higher for the MDS_{50} than for the MDS_{60} in the whole RI range. Sensitivities obtained in the phase measurements are summarized in Table 2.
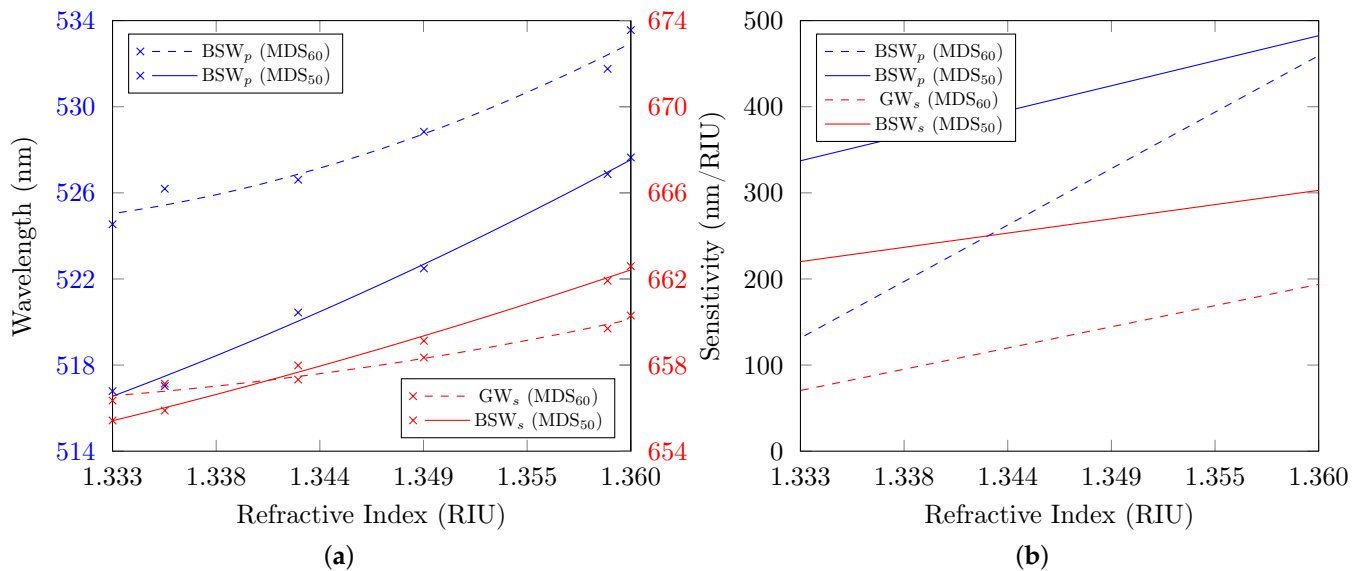
Figure 11. Dependencies of resonance wavelength (**a**) and RI sensitivity (**b**) on RI.

Table 2. Sensor performance parameters resulting from the phase measurements.

Sensor Parameters for Aqueous Analytes				
Structure	**MDS$_{60}$**		**MDS$_{50}$**	
Wave	**BSW$_p$**	**GW$_s$**	**BSW$_p$**	**BSW$_s$**
S (nm/RIU)	131.4–459.0	70.5–193.7	337.2–482.5	220.1–302.9
FWHM (nm)	4	1	12	1–2.1
FOM (RIU^{-1})	32.85–114.75	75.5–193.7	28.0–40.2	104.8–302.9

The FOM of 303 RIU^{-1} belongs to values that are close to those of other BSW-based sensors [4,19], but are not accessible by the SPR-based sensors [33].

4. Conclusions

In this paper, we demonstrated an efficient way of sensing of gaseous and aqueous analytes utilizing a MDS composed of six TiO$_2$/SiO$_2$ bilayers with a termination layer of TiO$_2$. We showed that for air, the GW can be excited by an *s*-polarized wave in the given wavelength range and we used a technique based on interference of reflected polarized waves to resolve the reflectance dips with their maximum depth. Theoretical analysis shows that the GW responses are with a linear shift of the resonance wavelength to small changes in the RI of the analyte, giving a constant RI sensitivity of 87 nm/RIU and FOM of 15.7 RIU^{-1}.

We performed experiments for analytes of aqueous solution of NaCl with the RI n_D in a range of 1.3331–1.3599, and we resolved resonance reflectance dips for BSWs excited by both *s*- and *p*-polarized waves for a specific MDS. We revealed very narrow reflectance dips whose widths can be affected by a limiting resolving power of a spectrometer. By a direct comparison of very narrow reflectance and phase responses for two designed and realized MDSs differing only in thicknesses of the termination layers, we showed that both RI sensitivity and FOM, which reach 544.3 nm/RIU and 303 RIU^{-1}, respectively, are higher for the case of MDS$_{50}$, thus making the structure more suitable for sensing applications.

Thus, we demonstrated not only very deep BSW-based resonances in two orthogonal polarizations, but also a very narrow resonance in a single polarization. Designs and realizations can be extended to MDSs supporting BSWs, which are characterized by a superior sensitivity and FOM, representing an effective alternative to other optical sensors. Moreover, based on the most recent theoretical results [34], phase response measurements can be extended using a setup not including a coupling prism.

Author Contributions: Conceptualization, R.K. and P.H.; methodology, R.K. and P.H.; software, R.K. and P.H.; validation, R.K. and P.H.; formal analysis, R.K. and P.H.; investigation, T.F., R.K., P.H., P.P. and J.S.; resources, R.K. and P.H.; data curation, R.K. and P.H.; writing—original draft preparation, R.K.; writing—review and editing, T.F, R.K., P.H.,P.P and J.S.; visualization, R.K. and P.H.; supervision, P.H.; project administration, T.F. and P.H.; funding acquisition, T.F. All authors have read and agreed to the published version of the manuscript.

Institutional Review Board Statement: Not applicable.

Informed Consent Statement: Not applicable.

Data Availability Statement: Not applicable.

Conflicts of Interest: The authors declare no conflict of interest.

References

1. Yeh, P. *Optical Waves in Layered Media*; John Wiley and Sons: Hoboken, NJ, USA, 2005.
2. Raether, H. *Surface Plasmons on Smooth and Rough Surfaces and on Gratings*; Springer: New York, NY, USA, 1988.
3. Wu, F.; Lyu, K.; Hu, S.; Yao, M.; Xiao, S. Ultra-large omnidirectional photonic band gaps in one-dimensional ternary photonic crystals composed of plasma, dielectric and hyperbolic metamaterial. *Opt. Mater.* **2021**, *111*, 110680. [CrossRef]
4. Giorgis, F.; Descrovi, E.; Summonte, C.; Dominici, L.; Michelotti, F. Experimental determination of the sensitivity of Bloch Surface Waves based sensors. *Opt. Express* **2010**, *18*, 8087–8093. [CrossRef] [PubMed]
5. Farmer, A.; Friedli, A.C.; Wright, S.M.; Robertson, W.M. Biosensing using surface electromagnetic waves in photonic band gap multilayers. *Sens. Actuators B Chem.* **2012**, *173*, 79–84. [CrossRef]
6. Kong, W.; Zheng, Z.; Wan, Y.; Li, S.; Liu, J. High-sensitivity sensing based on intensity-interrogated Bloch surface wave sensors. *Sens. Actuators B Chem.* **2014**, *193*, 467–471. [CrossRef]
7. Deng, C.Z.; Ho, Y.L.; Lee, Y.C.; Wang, Z.; Tai, Y.H.; Zyskowski, M.; Daiguji, H.; Delaunay, J.J. Two-pair multilayer Bloch surface wave platform in the near- and mid-infrared regions. *Appl. Phys. Lett.* **2019**, *115*, 091102. [CrossRef]
8. Gan, S.; Wang, H.; Liang, J.; Dai, X.; Xiang, Y. Ultra-Sensitive Refractive Index Sensors Based on Bloch Surface Waves with Transition Metal Dichalcogenides. *IEEE Sens. J.* **2019**, *19*, 8675–8680. [CrossRef]
9. Gryga, M.; Ciprian, D.; Hlubina, P. Sensing concept based on Bloch surface waves and wavelength interrogation. *Opt. Lett.* **2020**, *45*, 1096–1099. [CrossRef]
10. Gryga, M.; Ciprian, D.; Hlubina, P. Bloch surface wave resonance based sensors as an alternative to surface plasmon resonance sensors. *Sensors* **2020**, *20*, 5119. [CrossRef]
11. Goyal, A.K.; Pal, S. Design analysis of Bloch surface wave based sensor for haemoglobin concentration measurement. *Appl. Nanosci.* **2020**, *10*, 3639–3647. [CrossRef]
12. Guillermain, E.; Lysenko, V.; Orobtchouk, R.; Benyattou, T.; Roux, S.; Pillonnet, A.; Perriat, P. Bragg surface wave device based on porous silicon and its application for sensing. *Appl. Phys. Lett.* **2007**, *90*, 241116. [CrossRef]
13. Kang, X.B.; Wen, L.; Wang, Z.G. Design of guided Bloch surface wave resonance bio-sensors with high sensitivity. *Opt. Commun.* **2017**, *383*, 531–536. [CrossRef]
14. Kovalevich, T.; Belharet, D.; Robert, L.; Ulliac, G.; Kim, M.S.; Herzig, H.P.; Grosjean, T.; Bernal, M.P. Bloch surface waves at the telecommunicationwavelength with Lithium Niobate as top layer for integrated optics. *Appl. Opt.* **2019**, *58*, 1757–1762. [CrossRef] [PubMed]
15. Sinibaldi, A.; Rizzo, R.; Figliozzi, G.; Descrovi, E.; Danz, N.; Munzert, P.; Anopchenko, A.; Michelotti, F. A full ellipsometric approach to optical sensing with Bloch surface waves on photonic crystals. *Opt. Express* **2013**, *21*, 23331–23344. [CrossRef] [PubMed]
16. Li, Y.; Yang, T.; Song, S.; Pang, Z.; Du, G. Phase properties of Bloch surface waves and their sensing applications. *Appl. Phys. Lett.* **2013**, *103*, 041116. [CrossRef]
17. Li, Y.; Yang, T.; Pang, Z.; Du, G.; Song, S. Phase-sensitive Bloch surface wave sensor based on variable angle spectroscopic ellipsometry. *Opt. Express* **2014**, *22*, 21403–21410. [CrossRef]
18. Kaňok, R.; Hlubina, P.; Gembalová, L.; Ciprian, D. Efficient Optical Sensing Based on Phase Shift of Waves Supported by a One-Dimensional Photonic Crystal. *Sensors* **2021**, *21*, 6535. [CrossRef]
19. Hlubina, P.; Gryga, M.; Ciprian, D.; Pokorny, P.; Gembalova, L.; Sobota, J. High performance liquid analyte sensing based on Bloch surface wave resonances in the spectral domain. *Opt. Laser Technol.* **2022**, *145*, 107492. [CrossRef]
20. Chen, Y.H.; Shi, W.H.; Feng, L.; Xu, X.Y.; Shang-Guan, M.Y. Study on simultaneous sensing of gas concentration and temperature in one-dimensional photonic crystal. *Superlattices Microstruct.* **2019**, *131*, 53–58. [CrossRef]
21. Goyal, A.K.; Kumar, A.; Massoud, Y. Thermal Stability Analysis of Surface Wave Assisted Bio-Photonic Sensor. *Photonics* **2022**, *9*, 324. [CrossRef]
22. Pettersson, L.A.A.; Roman, L.S.; Inganäs, O. Modeling photocurrent action spectra of photovoltaic devices based on organic thin films. *J. Appl. Phys.* **1999**, *86*, 487–496. [CrossRef]
23. Daimon, M.; Masumura, A. Measurement of the refractive index of distilled water from the near-infrared region to the ultraviolet region. *Appl. Opt.* **2007**, *46*, 3811–3820. [CrossRef] [PubMed]
24. Polyanskiy, M.N. Refractive Index Database. Available online: http://refractiveindex.info (accessed on 1 July 2022) .
25. Sinibaldi, A.; Descrovi, E.; Giorgis, F.; Dominici, L.; Ballarini, M.; Mandracci, P.; Danz, N.; Michelotti, F. Hydrogenated amorphous silicon nitride photonic crystals for improved-performance surface electromagnetic wave biosensors. *Biomed. Opt. Express* **2012**, *3*, 2405–2410. doi: 10.1364/BOE.3.002405. [CrossRef] [PubMed]
26. Hlubina, P. Dispersive spectral-domain two-beam interference analysed by a fibre-optic spectrometer. *J. Mod. Opt.* **2004**, *51*, 537–547. [CrossRef]
27. Dubey, R.; Barakat, E.; Häyrinen, M.; Roussey, M.; Honkanen, S.K.; Kuittinen, M.; Herzig, H.P. Experimental investigation of the propagation properties of bloch surface waves on dielectric multilayer platforms. *J. Eur. Opt. Soc.* **2017**, *13*, 5. [CrossRef]
28. Guo, Y.; Ye, J.Y.; Divin, C.; Huang, B.; Thomas, T.P.; Baker, J.R.; Norris, T.B. Real-time biomolecular binding detection using a sensitive photonic crystal biosensor. *Anal. Chem.* **2010**, *82*, 211–5218. [CrossRef]
29. Gonzalez-Valencia, E.; Herrera, R.A.; Torres, P. Bloch surface wave resonance in photonic crystal fibers: Towards ultra-wide range refractive index sensors. *Opt. Express* **2019**, *27*, 8236–8545. [CrossRef]

30. Gonzalez-Valencia, E.; Villar, I.D.; Torres, P. Novel Bloch wave excitation platform based on few-layer photonic crystal deposited on D-shaped optical fiber. *Sci. Rep.* **2021**, *11*, 11266. [CrossRef]

31. Wan, X.Y.D.; Yan, Z. Simulation and analysis of surface plasmon resonance biosensor based on phase detection. *Sens. Actuators B Chem.* **2003**, *91*, 285–290.

32. Zhang, C.; Wang, R.; Min, C.; Zhu, S.; Yuan, X.C. Experimental approach to the microscopic phase-sensitive surface plasmon resonance biosensor. *Appl. Phys. Lett.* **2013**, *102*, 011114. [CrossRef]

33. Xu, Y.; Bai, P.; Zhou, X.; Akimov, Y.; Png, C.E.; Ang, L.K.; Knoll, W.; Wu, L. Optical Refractive Index Sensors with Plasmonic and Photonic Structures: Promising and Inconvenient Truth. *Adv. Opt. Mater.* **2019**, *7*, 1801433. [CrossRef]

34. Wu, F.; Liu, D.; Li, Y.; Li, H. Ultra-sensitive refractive index sensing enabled by a dramatic ellipsometric phase change at the band edge in a one-dimensional photonic crystal. *Opt. Express* **2022**, *30*, 29030–29043. [CrossRef]